Hilden, Panu; Shevchenko, Andriy

Extended depth of field of an imaging system with an annular aperture

Published in:
Optics Express

DOI:
10.1364/OE.484290

Published: 27/03/2023

Research Article | Vol. 31, No. 7 / 27 Mar 2023 / Optics Express 11102
Optics EXPRESS

Extended depth of field of an imaging system with an annular aperture

Panu Hildén[*] **and Andriy Shevchenko**

Department of Applied Physics, Aalto University, P.O Box 13500, FI-00076 Aalto, Finland
[*]*panu.hilden@aalto.fi*

Abstract: A common drawback of high-resolution optical imaging systems is a short depth of field. In this work, we address this problem by considering a $4f$-type imaging system with a ring-shaped aperture in the front focal plane of the second lens. The aperture makes the image consist of nearly non-diverging Bessel-like beams and considerably extends the depth of field. We consider both spatially coherent and incoherent systems and show that only incoherent light is able to form sharp and non-distorted images with extraordinarily long depth of field.

1. Introduction

In optical imaging, there is a trade-off between resolution and depth of field. In order to form a high-resolution image, a lens needs to have a high numerical aperture, due to which even a slight displacement of the object along the optical axis results in a blurred image. To overcome this problem, a number of methods have been developed. Many of them utilize phase masks to generate slowly diverging image fields [1–3]. Such phase masks are often combined with digital post-processing of the obtained images [4–7]. These methods include the incoherent digital holography that leads to a considerably extended effective depth of field [8,9]. An alternative approach is to use apodization [10–12]. Famously, an annular aperture can be used to extend the depth of focus of a lens (in contrast to the depth of field, the depth of focus is measured behind the lens, where light is focused). Such systems have been studied quite comprehensively [13–21], and have found applications, e.g., in scanning microscopes [22–24]. An annular aperture placed in the front focal plane of a lens extends the depth of focus by converting the focal field to a non-diverging zero-order Bessel beam [25–27]. This beam is a circularly symmetric version of more general propagation-invariant optical fields [28,29]. Other well-known examples are Mathieu and Weber beams [30,31] with elliptical and parabolic shapes, respectively. It has been recently shown that, in addition to these relatively simple beam configurations, infinitely many other non-diverging optical beams can be constructed by superposing multiple Bessel beams [32,33].

Obviously, by composing an image of Bessel beams, one can make it independent of the distance to the imaging system. This suggests that also the object can be freely moved along the optical axis without influencing the sharpness of the image. Therefore, the depth of field should be extraordinarily long. This can be achieved by using an infinitely thin annular aperture that acts as a spatial filter [32]. Such systems, however, have an infinitely low transmittance. In practice, the depth of field cannot be infinite because of a finite radius (R) of the imaging lens. If the focal length of the lens is f and the radius of the aperture is a, the depth of field is limited by fR/a.

In this work, we consider a $4f$-type imaging system (which is the simplest and probably also the most efficient imaging system that allows spatial filtering) with an annular aperture of a finite thickness. The images are therefore formed by nearly non-diverging Bessel-like beams. The performance of the system is studied, both theoretically and experimentally. We find that, when the illuminating light is spatially coherent, the Bessel beam sidelobes severely disturb the images,

#484290 https://doi.org/10.1364/OE.484290
Journal © 2023 Received 26 Dec 2022; revised 21 Feb 2023; accepted 21 Feb 2023; published 17 Mar 2023

Optics EXPRESS

e.g., making thin lines split into interference fringes. This is in agreement with Ref. [32], where the limit of an infinitely thin annular aperture is considered. With incoherent illumination, on the other hand, high-quality images with remarkably long depth of field are possible to obtain. In the calculations and experiments described below, we compare the performance of a system with an ordinary circular aperture to that with an annular aperture of the same outer diameter and reveal the advantages and drawbacks of the latter. The outer diameters are chosen to be equal for the systems to have the same highest spatial frequencies and comparable lateral resolutions. A larger circular aperture would result in a higher lateral resolution and a shorter depth of focus associated with the axial resolution of the system.

2. Theoretical description

Consider a $4f$-type imaging system shown in Fig. 1. A monochromatic light source illuminates a flat transparency (object), the image of which is formed by two confocal lenses and recorded by an array of detectors in the image plane (at the back focal plane of the second lens). If the object is displaced from the front focal plane of the first lens, $d_\mathrm{o} \neq f_1$, the image is blurred. However, using an annular aperture in the common focal plane of the two lenses can make the image sharper. The aperture acts as a spatial filter modifying the Fourier transform of the field produced by the first lens, $\tilde{U}_\mathrm{o}(kp/f_1, kq/f_1)$ [34]. An infinitely thin aperture with radius a would transmit only the plane wave components with radial wave number $k_r = ka/f_1$. The second lens then Fourier transforms the filtered field and forms an image composed only of the transmitted plane waves. In the paraxial approximation, the vector properties of light can be ignored, and the field in the image plane can be expressed as

$$\begin{aligned} U_\mathrm{i}(x,y) &= C \iint_{-\infty}^{\infty} \delta\left(\sqrt{p^2+q^2}-a\right) \tilde{U}_\mathrm{o}\left(\frac{kp}{f_1}, \frac{kq}{f_1}\right) \exp\left[-i\frac{k}{f_2}(xp+yq)\right] dpdq \\ &= C \oint \tilde{U}_\mathrm{o}\left(\frac{ka\cos\phi}{f_1}, \frac{ka\sin\phi}{f_1}\right) \exp\left[-i\frac{ka}{f_2}(x\cos\phi + y\sin\phi)\right] ad\phi, \end{aligned} \tag{1}$$

where $C \propto \exp[ik(d_\mathrm{o}+d_\mathrm{i})]$ is a complex constant and ϕ is the azimuthal angle. This expression takes the form of Whittaker's integral that is the general diffraction-free solution of the Helmholtz equation [26,28,33]. This means that the intensity distribution is independent of the distance from the second lens, which in Eq. (1) is $d_\mathrm{i} = f_2$. Indeed, the image turns out to be formed by non-diverging Bessel beams. Hence, if an infinitely thin ring-shaped aperture is used, the image should stay equally sharp when the object is moved along the optical axis. The depth of field should therefore be long.

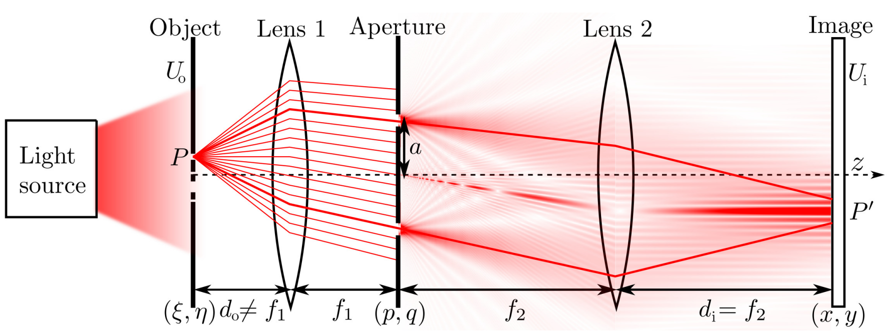

Fig. 1. An imaging system with an extended depth of field. The image is formed by Bessel-like beams owing to the presence of an annular aperture in the common focal plane of the two lenses.

Optics EXPRESS

The diffraction-free nature of the image field comes at a cost of removing most of the spatial-frequency components of the object field. Therefore, it is not clear, if the image will resemble the object. Let us calculate the image of a single point source P located in the object plane at a coordinate (ξ_P, η_P) (see Fig. 1). The object field can be written as $U_\mathrm{o}(\xi, \eta) = A_P\delta(\xi-\xi_P)\delta(\eta-\eta_P)$, where A_P is a constant describing the strength of the source. Using this expression in Eq. (1), we obtain

$$U_\mathrm{i}(x,y) = C\oint A_P \exp\left\{-i\frac{ka}{f_2}[(x-M\xi_P)\cos\varphi + (x-M\eta_P)\sin\varphi]\right\} a d\varphi. \tag{2}$$

The formed image is symmetric around point P' at $(x,y) = (M\xi_P, M\eta_P)$ in the image plane, i.e., around the geometrical-optics image of P, where $M = -f_2/f_1$ is the magnification of the imaging system including the image inversion. In Eq. (2), the complex amplitude A_P is independent of azimuthal angle ϕ, in which case, the Whittaker integral yields a zero-order Bessel beam [26], $U_\mathrm{i}(x,y) \propto J_0(kar_{P'}/f_2)$, where J_n is the n^{th} order Bessel function, and $r_{P'}$ is the radial distance from P'. That is to say, the point spread function (PSF) of the imaging system is a Bessel-like beam. Therefore, not only the PSF is diffraction-free, but also the images. Moreover, the mainlobe of the Bessel beam is narrower than that of the Airy pattern generated by conventional imaging system with the same numerical aperture (NA) (*cf.* the Rayleigh criterion of 0.38λ/NA for the Bessel beam to the conventional 0.61λ/NA [35]). However, as will be shown shortly, the energy of the Bessel beam is spread more to the sidelobes, which can considerably deteriorate the image quality.

For a realistic imaging system with a ring aperture of a finite thickness, the propagation of the object field through the setup is calculated in appendix A using the Fresnel diffraction theory. The resulting image field is found to be given by the expression

$$U_\mathrm{i}(x,y,d_\mathrm{o},d_\mathrm{i};\epsilon) = G(x,y,d_\mathrm{o},d_\mathrm{i};\epsilon) * U_\mathrm{g}(x,y), \tag{3}$$

where the geometrical-optics image of the object $U_\mathrm{g}(x,y) = U_\mathrm{o}(x/M, y/M)$ is convolved with the following PSF

$$\begin{aligned} G(x,y,d_\mathrm{o},d_\mathrm{i};\epsilon) &= C\left\{\int_0^1 \exp\left[-ik\frac{a^2\tau^2}{2}\left(\frac{f_1-d_\mathrm{o}}{f_1^2}+\frac{f_2-d_\mathrm{i}}{f_2^2}\right)\right] J_0\left(k\frac{ra\tau}{f_2}\right)\tau d\tau\right.\\ &\left.-\epsilon^2\int_0^1 \exp\left[-i\epsilon^2 k\frac{a^2\tau^2}{2}\left(\frac{d_\mathrm{o}-f_1}{f_1^2}+\frac{d_\mathrm{i}-f_2}{f_2^2}\right)\right] J_0\left(\epsilon k\frac{ra\tau}{f_2}\right)\tau d\tau\right\} \\ &= C\frac{\exp\left(-i\frac{u}{2}\right)}{u}\left\{U_1(u,v)+iU_2(u,v)-\epsilon^2[U_1(\epsilon^2 u,\epsilon v)+iU_2(\epsilon^2 u,\epsilon v)]\right\}. \end{aligned} \tag{4}$$

Here, C is a complex constant, U_1 and U_2 are the first- and second-order Lommel functions of two variables, u and v, and ϵ is the ratio of the inner and outer radii of the annular aperture (obscuration ratio). The variables u and v are, respectively, the normalized longitudinal and transverse coordinates defined as

$$u = ka^2\left(\frac{d_\mathrm{o}-f_1}{f_1^2}+\frac{d_\mathrm{i}-f_2}{f_2^2}\right), \tag{5}$$

$$v = k\frac{a}{f_2}r \quad \left(v_x = k\frac{a}{f_2}x, \quad v_y = k\frac{a}{f_2}y\right). \tag{6}$$

The longitudinal coordinate $u = 0$ corresponds exactly to the image plane, for which Eq. (4) simplifies to

$$G(0,v;\epsilon) = C\left[\frac{J_1(v)}{v} - \epsilon\frac{J_1(\epsilon v)}{v}\right]. \tag{7}$$

Optics EXPRESS

For an object in the front focal plane, $d_o = f_1$, the function G in Eq. (4) is equivalent to a focal field distribution of a single lens with an annular aperture [13] providing an extended depth of focus. From Eq. (5), it can be seen that a displacement of the object along z ($d_o \neq f_1$) has the same effect as the displacement of the detector array ($d_i \neq f_2$). Hence, the annular aperture also extends the *depth of field*.

Bessel beams produced by an annular aperture and a lens have been studied extensively [13–17]. In addition to reducing the effect of defocus, the annular aperture can influence other aberrations that the lenses may introduce [20]. It has also been shown that increasing the obscuration ratio ϵ decreases the transmitted energy by a factor $\int_0^\infty |G(u, v; \epsilon)|^2 v dv \propto (1 - \epsilon^2)$ [14]. The loss of light can be compensated for by increasing the detector integration time. The transmittance of the system can be improved either by applying structured illumination or by making use of a specifically designed polarization-coded aperture (such an aperture has been proposed in [36] for extending the depth of field without reducing the system's throughput). Additionally, an increase of ϵ narrows the mainlobe of the Bessel-like profile, improving the resolution, but also dispensing its energy to the sidelobes (see [15–17]). For example, an aperture with an obscuration ratio $\epsilon = 0.8$ produces a PSF corresponding to the Rayleigh criterion of $0.42\lambda/\mathrm{NA}$, but with only 17% of the energy concentrated in the mainlobe (*cf.* 84% for the Airy pattern). Extension of depth of field, narrowing of the mainlobe, and prominence of sidelobes are shown in Fig. 2, where the intensity distribution of the PSF ($|G|^2$) of the imaging system with the parameters f_1 = 11 mm, f_2 = 45 mm, a = 0.5 mm, λ = 632 nm, and obscuration ratios (a) $\epsilon = 0$ and (b) $\epsilon = 0.8$ are shown. The longitudinal coordinate corresponds to the displacement of object $\Delta z = d_o - f_1$.

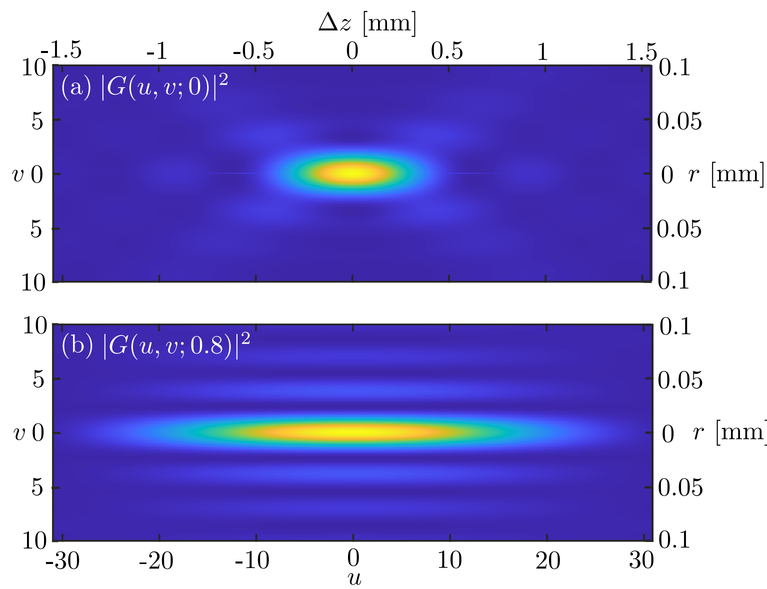

Fig. 2. The intensity distribution of PSF of the imaging system with obscuration ratio $\epsilon = 0$ and $\epsilon = 0.8$.

The influence of the sidelobes on the image quality can depend not only on ϵ, but also on spatial coherence of the light source [32]. In general, the intensity distribution in the image plane is given by $I_i = \langle |U_i|^2 \rangle$, where the angular brackets stand for time averaging. In the limits of fully spatially coherent and incoherent illumination, the intensity distribution in the image plane is calculated as

$$I_i^c(u, v_x, v_y; \epsilon) \propto |G(u, v_x, v_y; \epsilon) * U_g(v_x, v_y)|^2 \text{ and} \tag{8}$$

$$I_i^{ic}(u, v_x, v_y; \epsilon) \propto |G(u, v_x, v_y; \epsilon)|^2 * |U_g(v_x, v_y)|^2, \tag{9}$$

Optics EXPRESS

respectively [37]. The asterisk stands for convolution. The squared PSF in Eq. (9) is more localized (has smaller sidelobes) and should lead to better images. As an example, let us consider imaging of a thin and long line, such that $U_g(v_x, v_y) = A_0\delta(v_x)$. In appendix B, the image formed by a coherent light is found to be given by

$$\mathcal{I}^{c}_{\mathrm{line}}(v_x;\epsilon) = (1-\epsilon)^2\cos^2\left(\frac{1+\epsilon}{2}v_x\right)\mathrm{sinc}^2\left(\frac{1-\epsilon}{2}v_x\right), \tag{10}$$

where $\mathcal{I}(v_x;\epsilon) = I(v_x;\epsilon)/I(0;0)$ is a normalized intensity distribution. Here, the intensity distribution is obtained for an infinitely long line. A finite line, however, will yield essentially the same result as long as its diffraction pattern at the focal plane (along the line) is smaller than the annular aperture. It is quite remarkable that the obtained distribution is the same as the one found in a double-slit experiment with slits of width $(1-\epsilon)a$ and separation $(1+\epsilon)a$. Hence, for a high obscuration ratio ϵ, the light does not retain a geometric image of the line, but forms intensity fringes (see the blue solid line in Fig. 3(a)). Obviously, the approach does not work with spatially coherent light. For comparison, the image of a line formed by an incoherent light is described by

$$\mathcal{I}^{\mathrm{ic}}_{\mathrm{line}}(v_x;\epsilon) = \frac{3\pi}{8}\left[\frac{H_1(2v_x)+\epsilon H_1(\epsilon 2v_x)}{v_x^2} - 4\epsilon\int_{v_x}^{\infty}\frac{J_1(v)J_1(\epsilon v)}{v\sqrt{v^2-v_x^2}}dv\right], \tag{11}$$

as shown in appendix B (see also Ref. [18]). This function is introduced by the orange solid line in Fig. 3(a). Without obscuration ($\epsilon = 0$), the incoherent image is given by the first-order Struve function $H_1(2v_x)/v_x^2$ shown in Fig. 3(a) by the orange dashed line alongside the coherent counterpart shown by the blue dashed line. As shown in appendix B, the amount of light at the center $I_{\mathrm{line}}(0;\epsilon)$ depends on ϵ in accordance with

$$\mathcal{I}^{\mathrm{c}}_{\mathrm{line}}(0;\epsilon) = (1-\epsilon)^2 \text{ and} \tag{12}$$

$$\mathcal{I}^{\mathrm{ic}}_{\mathrm{line}}(0;\epsilon) = 1+\epsilon^3+(1-\epsilon^2)K(\epsilon^2)-(1+\epsilon^2)E(\epsilon^2) \tag{13}$$

for coherent and incoherent light, respectively. Here, K and E are the complete elliptic integrals of the first and second kind, respectively. The equations satisfy the inequality $\mathcal{I}^{\mathrm{c}}_{\mathrm{line}}(0;\epsilon)<\mathcal{I}^{\mathrm{ic}}_{\mathrm{line}}(0;\epsilon)$ for $\epsilon \in (0,1)$, as shown in Fig. 3(b). The incoherent light is obviously advantageous for this type of imaging, as it does not spread as much as the coherent light. For example, for $\epsilon = 0.8$, the incoherent image retains 3.5 times more light at $x = 0$ compared to the coherent image.

Equations (8) and (9) can be used to simulate images of arbitrary objects. To accelerate computations, the PSF can be expanded using Zernike's method [39]. The expanded PSF is

$$\begin{aligned} G(u,v;\epsilon) &= C\sqrt{\frac{2\pi}{uv^2}} \\ &\times\sum_{n=0}^{\infty} i^n(2n+1)\left[\exp\left(-i\frac{u}{4}\right)J_{n+\frac{1}{2}}\left(\frac{u}{4}\right)J_{2n+1}(v) - \exp\left(-i\frac{\epsilon^2 u}{4}\right)J_{n+\frac{1}{2}}\left(\frac{\epsilon^2 u}{4}\right)J_{2n+1}(\epsilon v)\right]. \end{aligned} \tag{14}$$

The imaging capabilities of the system with incoherent illumination are demonstrated in Fig. 4, using a digital map of squares (512×512 pixels) of many shades and sizes as an object ("texmos2.s512" from the USC-SIPI image database [38]). For the simulation, we used the parameters $f_1 = 11$ mm, $f_2 = 45$ mm, $a = 0.5$ mm, and $\epsilon = 0$ and 0.8 for Figs. 4(a) - (c) and (d) - (g), respectively. The object is shifted along z by $\Delta z = d_o - f_1$ equal to 0, 0.4 mm, and 0.8 mm. For $\epsilon = 0$, the shift leads to considerable blurring of the image and loss of the information (Fig. 4(a)-(d)). With $\epsilon = 0.8$, on the other hand, the contrast is lower, but the shift does not change the sharpness of the image, demonstrating a remarkable depth of field. The contrast can be increased back by post-processing the image, e.g., by re-scaling its brightness or by a more precise deconvolution technique [40].

Optics EXPRESS

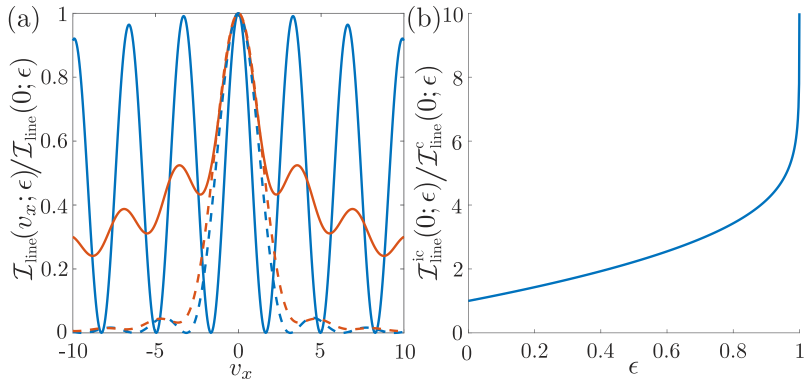

Fig. 3. (a) Transverse intesity distribution of the image of an infinitely thin and long line obtained with the imaging system of Fig. 1 with (solid lines) and without (dashed lines) the central obscuration, using both coherent (blue) and incoherent (orange) light sources. The obscuration ratio is $\epsilon = 0.9$. (b) The ratio of light intensities at the center of the image for incoherent optical system to that of a coherent system as a function of ϵ.

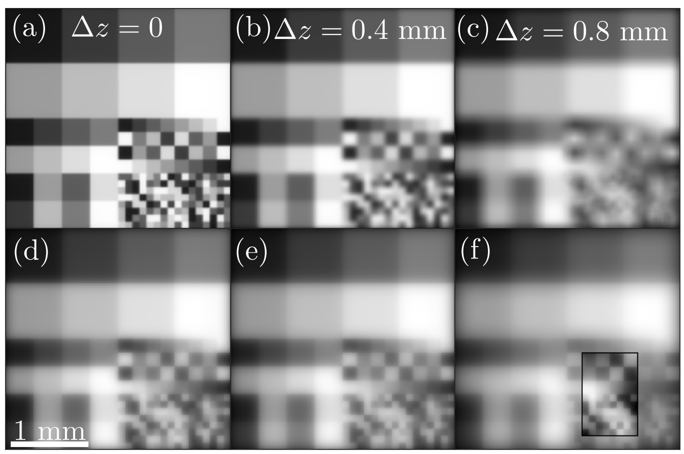

Fig. 4. Simulated images of an array of squares ("texmos2.s512" [38]) obtained for an incoherent imaging system with $\epsilon = 0$ [(a) - (c)] and $\epsilon = 0.8$ [(d) - (f)]. The object is displaced from the focal plane of the first lens by Δz equal to 0, 0.4 mm, and 0.8 mm. In (f), a part of the image is modified to improve the contrast.

3. Experiments

An imaging system corresponding to Fig. 1 was built to experimentally verify our theoretical predictions. As a coherent light source, a HeNe laser (Uniphase 1135P) with a center wavelength of 633 nm was used. For incoherent illumination, we used an LED (Thorlabs M625L3) with a 632-nm center wavelength. The objects and the annular aperture were made by patterning an aluminium film on glass. The diameter and thickness of the annular aperture are 1 mm and 100 µm, respectively, corresponding to the obscuration ratio $\epsilon = 0.8$. For reference images, the annular aperture was replaced with an iris (Thorlabs ID25/M) of 1-mm diameter. The setup was used to form magnified images ($M \approx -4$) using a lens and a microscope objective with the focal lengths $f_1 = 11$ mm and $f_2 = 45$ mm, respectively. In addition, a demagnifying setup ($M \approx -1/2$) was tested, in which case we had $f_1 = 45$ mm and $f_2 = 25$ mm. The two systems have a resolution (the $1/e$ width of the PSF without magnification) $\delta r = 5.2$ μm (magnifying setup) and $\delta r = 21.4$ μm (demagnifying setup), corresponding to Rayleigh ranges z_R of approximately 140 μm and 2.3 mm, respectively. The images were recorded with a camera Basler acA1920-25uc. All the images were normalized such that the brightest pixel appears completely white.

Figure 5 shows images of a ring-shaped slit with a diameter of 200 μm and a width of 20 μm taken by using the magnifying setup with coherent illumination. The images are obtained without (Fig. 5(a)) and with the annular aperture (Fig. 5(b)) between the two lenses. The aperture is seen to destroy the image by splitting it into many interference rings. The pattern corresponds to the theoretical pattern shown in Fig. 5(c); it was obtained by solving Eq. (8). In fact, the observed Poisson spot at the center of the pattern is so bright that Figs. 5(b) and (c) had to be severely saturated in order to see the outer rings. This example clearly shows that, despite an increased depth of field, the approach does not work when used with coherent illumination.

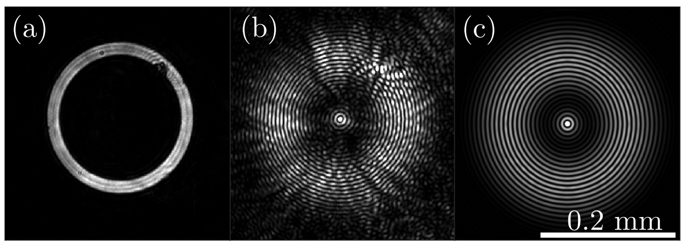

Fig. 5. Images of a ring-shaped slit in a metal film taken by the magnifying imaging system with coherent illumination, when the annular aperture was (a) removed from and (b) inserted into the system. In (c), the calculated image that corresponds to case (b) is shown.

Next, images of the same ring-shaped slit were taken using incoherent light. They are shown in Figs. 6(a) and 6(d) for the system used with the annular aperture and the iris, respectively. The annular aperture in this case does not destroy the image at all. The extended depth of field due to the annular aperture is showcased by the images in Figs. 6(b) and 6(c) obtained with the object shifted by $\Delta z = 0.4$ mm ($\Delta z/z_R \approx 3$) and $\Delta z = 0.8$ mm, respectively, away from the front focal plane of the system. In both images, the slit edges are clearly seen, even though a smooth white background appears when Δz increases. In contrast, when using the iris, the defocused images are significantly blurred (see Figs. 6(e) and (f)). In order to verify these results by calculations, the images in Figs. 6(a) - (f) were reproduced by solving Eq. (13). They are shown in Figs. 6(g)-(l) on the matching order. The calculated images are in agreement with the experimental ones. This suggests that, if needed, the PSF given by Eq. (4) can be used to deconvolve the experimentally obtained images and completely get rid of the parasitic background. For the imaging system with the annular aperture, the intensity at the center of the PSF decreases by 20 % at distances $\Delta z = \pm 0.44$ mm, which is often considered as an acceptable limit [41], yielding the total depth of field of 0.88 mm (*cf.* 0.32 mm for a circular aperture). However, this quantitative measure of the depth of field is not exact, as it fails to take into account the qualitive difference of the shapes of the PSF in the two cases (see Fig. 2) and their influence on the defocused images demonstrated in Fig. 6.

In order to show that not only narrow slits can be imaged with the system, we took images of an opaque logo of Aalto University. The logo is formed by 20 μm thick aluminum stripes. The images obtained by using incoherent illumination with the annular aperture and with the equal-radius iris are shown in Figs. 7(a) - (c) and 7(d) - (f), respectively. In order to demonstrate that the depth of field is extended symmetrically in both directions, we moved the object this time towards the imaging system, by 0.4 and 0.8 mm. In the presence of the annular aperture, the image remains sharp (Figs. 7(b) and (c)). The contrast of the image can be improved by

Optics EXPRESS

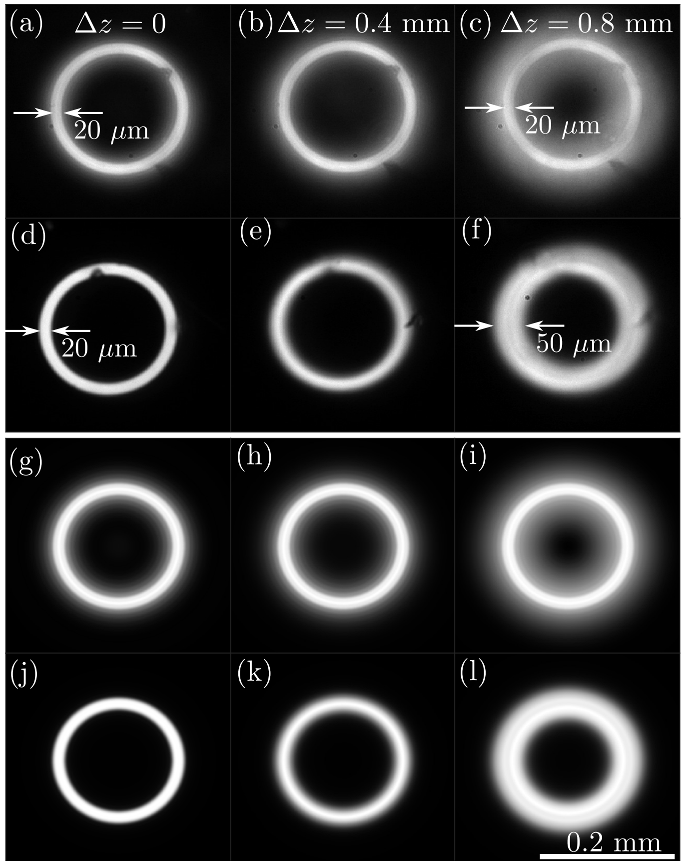

Fig. 6. Images of ring-shaped slit obtained by using the magnifying imaging setup with incoherent illumination and the annular aperture (a) - (c) or the iris (d) - (f) used in the system. The corresponding simulated versions are shown in (g) - (l) in the same order. The columns of images, starting from the left, are obtained for Δz = 0, 0.4 mm, and 0.8 mm, respectively.

a computer post-processing. With the iris, the image becomes blurred (Figs. 7(e) and (f)), as before.

We have also tested the demagnifying setup by taking images of a 100 µm thick ring-shaped slit with a 1 mm diameter. The images obtained in the presence of the annular aperture and the iris are shown in Figs. 8(a) - (c) and 8(d) - (f), respectively. To evaluate the depth of field, the object was moved by 6 mm ($\Delta z/z_R \approx 3$) and 12 mm away from focal plane of the first lens. Based on the longitudinal intensity distribution of the PSF, the depth of field with the annular aperture is 14.7 mm (*cf.* 5.3 mm for the circular aperture). The demagnifying setup has a much longer depth of field, but the factor by which the annular aperture extends the depth of field appears to be the same as in the magnifying setup. Indeed, the extension of the depth of focus for fields of the form given by Eq. (4) is determined only by the obscuration ration ϵ.

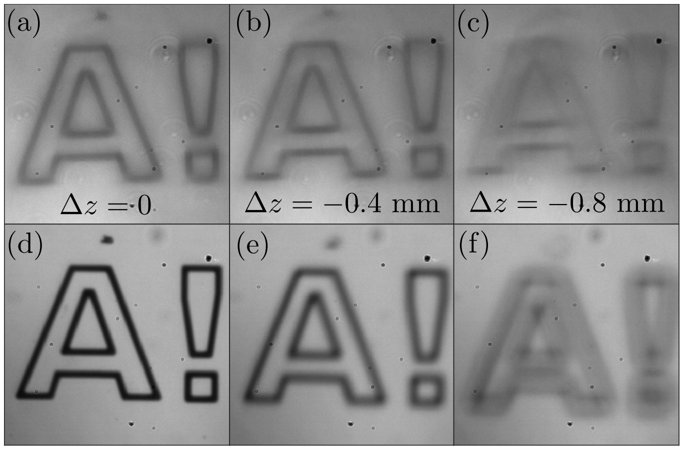

Fig. 7. Images of an opaque logo of Aalto University obtained using the magnifying imaging setup and the incoherent light source. The logo is formed by 20 µm thick aluminum stripes. In (a) - (c) and (d) - (f), the images were taken in the presence of the annular aperture and the iris, respectively. The columns of images, starting from the left, are obtained at $\Delta z = 0$, -0.4 mm, and -0.8 mm, respectively.

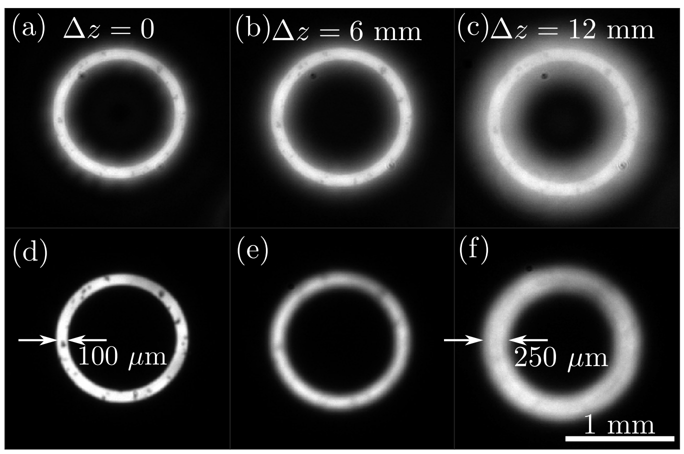

Fig. 8. Images of ring-shaped slit obtained by using the demagnifying imaging setup with incoherent illumination and the annular aperture (a) - (c) or the iris (d) - (f) used in the system. The columns of images, starting from the left, are obtained at $\Delta z = 0$, 6 mm, and 12 mm, respectively.

4. Conclusion

We have considered a $4f$-type imaging system with an extended depth of field achieved by using an annular aperture in the common focal plane of the two lenses. We have shown, both analytically and experimentally, that the considered system generates images composed of Bessel-like beams, resulting in an extraordinarily long depth of field. It was also shown that the system used with spatially incoherent illumination produces nearly non-diverging high-quality images, whereas coherent illumination distorts the images by splitting them into interference fringes. The system is relatively compact and consists of only standard optical components, which makes the device easy to build and use. The results obtained in this work can be used to design many practical

Optics EXPRESS

devises with the extended depth of field, such as high-resolution microscopes and optical systems imaging three-dimensional objects.

A. Field propagation through the imaging system

The field in the object plane, $U_\text{o}(\xi, \eta)$, transmitted through the imaging system of Fig. 1 results in a field $U_\text{i}(x, y)$ in the image plane given by

$$U_\text{i} = h(d_\text{i}) * t_\text{L}(f_2)(h(f_2) * t_\text{A}\{h(f_1) * t_\text{L}(f_1)[h(d_\text{o}) * U_\text{o}]\}), \tag{15}$$

where t_A is the amplitude transmission function of the aperture, $t_\text{L} = \exp(-ikr^2/2f)$ is the transmission function of the lens with focal length f, and $h(z)$ is the PSF of free-space propagation over a distance d, which, using the Fresnel approximation, is written as

$$h(d) = \frac{k}{i2\pi d} \exp\left[ik\left(d + \frac{r^2}{2d}\right)\right]. \tag{16}$$

For a field V propagating from a plane n to a plane $n+1$ in free space, we obtain

$$\begin{aligned} h(d) * V = & \frac{k}{i2\pi d} \exp\left[ik\left(d + \frac{r_{n+1}^2}{2d}\right)\right] \\ & \times \iint_{-\infty}^{\infty} V(x_n, y_n) \exp\left(ik\frac{r_n^2}{2d}\right) \exp\left[-i\frac{k}{d}(x_{n+1}x_n + y_{n+1}y_n)\right] dx_n dy_n \\ = & \frac{k}{i2\pi d} \exp\left[ik\left(d + \frac{r_{n+1}^2}{2d}\right)\right] \mathcal{F}_d\left[V(x_n, y_n) \exp\left(ik\frac{r_n^2}{2d}\right)\right], \end{aligned} \tag{17}$$

where $\mathcal{F}_d[W(x_n, x_n)] = \tilde{W}(k_x, k_y)$ is the two-dimensional Fourier transform of W evaluated at $(k_x, k_y) = (kx_{n+1}/d, ky_{n+1}/d)$. Equation 17 is the Fresnel-Kirchhoff diffraction integral.

In order to solve Eq. (15), we start considering transformation of the field due to a single-lens imaging system. By applying Eq. (17) twice, alongside the convolution theorem, the image of object field $V_\text{o}(x_n, y_n)$ can be expressed as

$$\begin{aligned} V_\text{i} & = h(d_\text{i}) * t_\text{L}(f)[h(d_\text{o}) * V_\text{o}] \\ & = -\frac{k^4}{(2\pi)^4 d_\text{i}^3 d_\text{o}} \exp\left[ik\left(d_\text{i} + d_\text{o} + \frac{r_{n+2}^2}{2d_\text{i}}\right)\right] \\ & \times \mathcal{F}_{d_\text{i}}\left[\exp\left(ik\frac{r_{n+1}^2}{2}\psi\right)\right] * \mathcal{F}_{d_\text{i}}\left[\mathcal{F}_{d_\text{o}}\left[V_\text{o}(x_n, y_n) \exp\left(ik\frac{r_n^2}{2d_\text{o}}\right)\right]\right], \end{aligned} \tag{18}$$

where $\psi = d_\text{o}^{-1} + d_\text{i}^{-1} - f^{-1}$ is the focusing error. The double Fourier transform just invert and scale the function $\mathcal{F}_D\left[\mathcal{F}_d[W(x_n, y_n)]\right] \propto W\left(-\frac{d}{D}x_{n+2}, -\frac{d}{D}y_{n+2}\right)$, whereas Fourier transform of $\exp\left(ikr_{n+1}^2\psi/2\right)$ can be calculated as a Hankel transform, yielding

$$\begin{aligned} \mathcal{F}_{d_\text{i}}\left[\exp\left(ik\frac{r_{n+1}^2}{2}\psi\right)\right] & = 2\pi \int_0^\infty \exp\left(ik\frac{r_{n+1}^2}{2}\psi\right) J_0\left(k\frac{r_{n+2}r_{n+1}}{d_\text{i}}\right) r_{n+1}dr_{n+1} \\ & = \frac{i2\pi}{k\psi} \exp\left(-ik\frac{r_{n+2}^2}{2{d_\text{i}}^2\psi}\right) \end{aligned} \tag{19}$$

if $\psi \neq 0$. If $\psi = 0$, Eq. (19) yields the Dirac delta-function, and consequently, Eq. (18) yields a perfectly sharp image (if the lens aperture is neglected). Inserting the evaluated Fourier

Optics EXPRESS

transforms into Eq. (18), we obtain

$$\begin{aligned} V_{\mathrm{i}} &= \frac{kd_{\mathrm{o}}}{i2\pi d_{\mathrm{i}}^{3}\psi} \exp\left[ik\left(d_{\mathrm{i}} + d_{\mathrm{o}} + \frac{r_{n+2}^{2}}{2d_{\mathrm{i}}}\right)\right] \\ &\times \exp\left(-ik\frac{r_{n+2}^{2}}{2{d_{\mathrm{i}}}^{2}\psi}\right) * \left[V_{\mathrm{o}}\left(-\frac{d_{o}}{d_{\mathrm{i}}}x_{n+2}, -\frac{d_{o}}{d_{\mathrm{i}}}y_{n+2}\right)\exp\left(ik\frac{r_{n+2}^{2}d_{o}}{2d_{\mathrm{i}}^{2}}\right)\right] \\ &= \frac{kd_{\mathrm{o}}}{i2\pi d_{\mathrm{i}}^{3}\psi} \exp\left[ik\left(d_{\mathrm{i}} + d_{\mathrm{o}} + \frac{r_{n+2}^{2}}{2d_{\mathrm{i}}}\right)\right] \exp\left(-ik\frac{r_{n+3}^{2}}{2d_{\mathrm{i}}^{2}\psi}\right) \times \iint_{-\infty}^{\infty} V_{\mathrm{o}}\left(-\frac{d_{o}}{d_{\mathrm{i}}}x_{n+2}, -\frac{d_{o}}{d_{\mathrm{i}}}y_{n+2}\right) \\ &\exp\left[ik\frac{r_{n+2}^{2}}{2d_{\mathrm{i}}^{2}}\left(d_{\mathrm{o}} - \psi^{-1}\right)\right] \exp\left[\frac{ik}{{d_{\mathrm{i}}}^{2}\psi}\left(x_{n+3}x_{n+2} + y_{n+3}y_{n+2}\right)\right] dx_{n+2}dy_{n+2}. \end{aligned} \tag{20}$$

Using the change of variables $X_n = -d_{\mathrm{o}}x_{n+2}/d_{\mathrm{i}}$, $Y_n = -d_{\mathrm{o}}y_{n+2}/d_{\mathrm{i}}$, $X_{n+1} = x_{n+3} = -d_{\mathrm{i}}X_n/d_{\mathrm{o}}$, and $Y_{n+1} = y_{n+3} = -d_{\mathrm{i}}Y_n/d_{\mathrm{o}}$, Eq. (20) can be rewritten as

$$\begin{aligned} V_{\mathrm{i}} &= \frac{k}{i2\pi d_{\mathrm{o}}d_{\mathrm{i}}\psi} \exp\left[ik\left(d_{o} + d_{i}\right)\right] \exp\left[ik\frac{R_{n+1}^{2}}{2d_{\mathrm{i}}^{2}}\left(d_{\mathrm{i}} - \psi^{-1}\right)\right] \\ &\times \iint_{-\infty}^{\infty} V_{\mathrm{o}}\left(X_n, Y_n\right) \exp\left[ik\frac{R_{n}^{2}}{2d_{\mathrm{o}}^{2}}\left(d_{\mathrm{o}} - \psi^{-1}\right)\right] \exp\left[\frac{ik}{d_{\mathrm{o}}d_{\mathrm{i}}\psi}\left(X_{n+1}X_n + Y_{n+1}Y_n\right)\right] dX_n dY_n \\ &= \frac{k}{i2\pi d_{\mathrm{o}}d_{\mathrm{i}}\psi} \exp\left[ik\left(d_{\mathrm{o}} + d_{i}\right)\right] \exp\left[ik\frac{R_{n+1}^{2}}{2d_{\mathrm{i}}^{2}}\left(d_{\mathrm{i}} - \psi^{-1}\right)\right] \\ &\times F_{d_{\mathrm{o}}d_{i}\psi}\left[V_{o}\left(X_n, Y_n\right) \exp\left(ik\frac{R_{n}^{2}}{2d_{\mathrm{o}}}\frac{d_{\mathrm{i}}^{-1} - f^{-1}}{\psi}\right)\right]. \end{aligned} \tag{21}$$

For $d_{\mathrm{i}} = f$ and $d_{\mathrm{o}} = f$, Eq. (21) simplifies to the following expressions

$$V_{\mathrm{i}}(d_{\mathrm{i}} = f) = \frac{k}{i2\pi f} \exp\left[ik\left(d_{\mathrm{o}} + f\right)\right] \exp\left[ik\frac{R_{n+1}^{2}}{2f^{2}}\left(f - d_{\mathrm{o}}\right)\right] F_{f}\left[V_{\mathrm{o}}\left(X_n, Y_n\right)\right], \tag{22}$$

$$V_{\mathrm{i}}(d_{\mathrm{o}} = f) = \frac{k}{i2\pi f} \exp\left[ik\left(f + d_{\mathrm{i}}\right)\right] F_{f}\left[V_{\mathrm{o}}\left(X_n, Y_n\right) \exp\left[ik\frac{R_{n}^{2}}{2f^{2}}(f - d_{\mathrm{i}})\right]\right], \tag{23}$$

respectively.

The first lens of the imaging system transforms the field according to Eq. (22) with transverse coordinates $(X_1, Y_1) = (\xi, \eta)$ and $(X_2, Y_2, R_2) = (p, q, \rho)$. Therefore, the field U_{f} incident on the annular aperture is given by

$$U_{\mathrm{f}}(p, q) = \frac{k}{i2\pi f_1} \exp\left[ik\left(d_{\mathrm{o}} + f_1\right)\right] \exp\left[ik\frac{\rho^{2}}{2f_1^{2}}\left(f_1 - d_{\mathrm{o}}\right)\right] F_{f_1}\left[U_{\mathrm{o}}\left(\xi, \eta\right)\right]. \tag{24}$$

The second lens transforms the field according to Eq. (23). Thus, the image field given by Eq. (15) can be expressed as

$$U_{\mathrm{i}}(x, y) = \frac{k}{i2\pi f_2} \exp\left[ik\left(f_2 + d_{\mathrm{i}}\right)\right] F_{f_2}\left[t_{\mathrm{A}}(\rho)U_{\mathrm{f}}\left(p, q\right) \exp\left[ik\frac{\rho^{2}}{2f_2^{2}}\left(f_2 - d_{\mathrm{i}}\right)\right]\right]. \tag{25}$$

Optics EXPRESS

We recall that $F_{f_2}[W(p,q)] = F_{f_2}[W(X_2,Y_2)] = \tilde{W}(kX_3/f_2, kY_3/f_2) = \tilde{W}(kx/f_2, ky/f_2)$. Inserting Eq. (24) into Eq. (25) yields

$$\begin{aligned} U_{\mathrm{i}} = &-\frac{k^2}{(2\pi)^2 f_1 f_2}\exp\left[ik\left(d_{\mathrm{o}}+f_1+f_2+d_{\mathrm{i}}\right)\right] \\ &\times F_{f_2}\left[t_{\mathrm{A}}(\rho)\exp\left[ik\frac{\rho^2}{2f_1^2}\left(f_1-d_{\mathrm{o}}\right)\right]F_{f_1}\left[U_{\mathrm{o}}(\xi,\eta)\right]\exp\left[ik\frac{\rho^2}{2f_2^2}\left(f_2-d_{\mathrm{i}}\right)\right]\right]. \end{aligned} \tag{26}$$

Using the convolution theorem, the expression for the image field can be rewritten as

$$\begin{aligned} U_{\mathrm{i}} &= -\frac{k^4}{(2\pi)^4 f_1 f_2^3}\exp\left[ik\left(d_{\mathrm{o}}+f_1+f_2+d_{\mathrm{i}}\right)\right] \\ &\times F_{f_2}\left[t_{\mathrm{A}}(\rho)\exp\left[ik\frac{\rho^2}{2}\left(\frac{f_1-d_{\mathrm{o}}}{f_1^2}+\frac{f_2-d_{\mathrm{i}}}{f_2^2}\right)\right]\right] * F_{f_2}\left[F_{f_1}\left[U_{\mathrm{o}}(\xi,\eta)\right]\right] \\ &= G(x,y,d_{\mathrm{o}},d_{\mathrm{i}};\epsilon) * U_{\mathrm{o}}(x/M, y/M), \end{aligned} \tag{27}$$

where $M = -f_2/f_1$ is the magnification of the imaging system. For an annular aperture with the outer and inner radii a and ϵa, respectively, the Fourier transform determining the PSF of the system G is

$$\begin{aligned} G &= \frac{k^2}{2\pi M f_2^2}\exp\left[ik\left(d_{\mathrm{o}}+f_1+f_2+d_{\mathrm{i}}\right)\right]\int_{\epsilon a}^{a}\exp\left[ik\frac{\rho^2}{2}\left(\frac{d_{\mathrm{o}}-f_1}{f_1^2}+\frac{d_{\mathrm{i}}-f_2}{f_2^2}\right)\right]J_0\left(k\frac{r\rho}{f_2}\right)\rho d\rho \\ &= C\left\{\int_0^1 \exp\left[-ik\frac{a^2\tau^2}{2}\left(\frac{f_1-d_{\mathrm{o}}}{f_1^2}+\frac{f_2-d_{\mathrm{i}}}{f_2^2}\right)\right]J_0\left(k\frac{ra\tau}{f_2}\right)\tau d\tau\right. \\ &\left.-\epsilon^2\int_0^1 \exp\left[-i\epsilon^2 k\frac{a^2\tau^2}{2}\left(\frac{d_{\mathrm{o}}-f_1}{f_1^2}+\frac{d_{\mathrm{i}}-f_2}{f_2^2}\right)\right]J_0\left(\epsilon k\frac{ra\tau}{f_2}\right)\tau d\tau\right\}. \end{aligned} \tag{28}$$

Here, $C = (ka)^2\exp[ik(d_{\mathrm{o}}+f_1+f_2+d_{\mathrm{i}})]/(2\pi M f_2^2)$ is a complex constant.

B. Image of a line

If coherent illumination is used and the imaging system is ideally aligned, the image of an infinitely thin and long line can be found by inserting the corresponding geometric image field $U_{\mathrm{g}} = A_0\delta(v_x)$ and the PSF given by Eq. (7) into Eq. (8). The intensity distribution in the image plane is found to be

$$\begin{aligned} I^{\mathrm{c}}_{\mathrm{line}}(v_x, v_y;\epsilon) &\propto \left|A_0\int_{-\infty}^{\infty} G\left(0,\sqrt{v_x^2+v_y^2};\epsilon\right)dv_y\right|^2 \\ &\propto \left|2A_0 C\int_{v_x}^{\infty}\left[\frac{J_1(v)}{v}-\epsilon\frac{J_1(\epsilon v)}{v}\right]\frac{v}{\sqrt{v^2-v_x^2}}dv\right|^2 \end{aligned} \tag{29}$$

for $v_x \geq 0$ ($I^{\mathrm{c}}_{\mathrm{line}}(-v_x) = I^{\mathrm{c}}_{\mathrm{line}}(v_x)$). In Eq. (29), a substitution $v_y = \sqrt{v^2 - v_x^2}$ has been used in order to solve the integral, yielding

$$\begin{aligned} I^{\mathrm{c}}_{\mathrm{line}}(v_x;\epsilon) &\propto 4|A_0C|^2\left(\frac{\sin v_x - \sin\epsilon v_x}{v_x}\right)^2 \\ &\propto 4|A_0C|^2(1-\epsilon)^2\cos^2\left(\frac{1+\epsilon}{2}v_x\right)\mathrm{sinc}^2\left(\frac{1-\epsilon}{2}v_x\right). \end{aligned} \tag{30}$$

If the illumination is incoherent, the intensity distribution is given by Eq. (9), resulting in the expression

$$\begin{aligned} I^{\mathrm{ic}}_{\mathrm{line}}(v_x;\epsilon) &\propto 2|A_0C|^2 \int_{v_x}^{\infty} \left[\frac{J_1(v)}{v} - \epsilon\frac{J_1(\epsilon v)}{v}\right]^2 \frac{v}{\sqrt{v^2 - v_x^2}} dv \\ &\propto |A_0C|^2 \left[\frac{H_1(2v_x) + \epsilon H_1(\epsilon 2v_x)}{v_x^2} - 4\epsilon \int_{v_x}^{\infty} \frac{J_1(v)J_1(\epsilon v)}{v\sqrt{v^2 - v_x^2}} dv\right], \end{aligned} \tag{31}$$

where H_1 is the first-order Struve function. At the position of the geometric image of the line ($v_x = 0$), Eq. (31) simplifies to

$$\begin{aligned} I^{\mathrm{ic}}_{\mathrm{line}}(0;\epsilon) &\propto 2|A_0C|^2 \int_{0}^{\infty} \left[\frac{J_1(v)}{v} - \epsilon\frac{J_1(\epsilon v)}{v}\right]^2 dv \\ &\propto \frac{8}{3\pi}|A_0C|^2 \left[1 + \epsilon^3 + (1-\epsilon^2)K(\epsilon^2) - (1+\epsilon^2)E(\epsilon^2)\right], \end{aligned} \tag{32}$$

where K and E are the complete elliptic integrals of the first and second kind, respectively.

Funding. Jenny ja Antti Wihurin Rahasto (00210075); Academy of Finland (308394); Aalto Science Institute AScI; Academy of Finland Flagship Programme, Photonics Research and Innovation (PREIN).

Disclosures. The authors declare no conflicts of interest.

Data availability. Data underlying the results presented in this paper are not publicly available at this time but may be obtained from the authors upon reasonable request.

References

1. A. Kolodziejczyk, S. Bará, Z. Jaroszewicz, and M. Sypek, “The Light Sword Optical Element— a New Diffraction Structure with Extended Depth of Focus,” J. Mod. Opt. **37**(8), 1283–1286 (1990).
2. N. Davidson, A. A. Friesem, and E. Hasman, “Holographic Axilens: High Resolution and Long Focal Depth,” Opt. Lett. **16**(7), 523–525 (1991).
3. E. Ben-Eliezer, Z. Zalevsky, E. Marom, and N. Konforti, “All-Optical Extended Depth of Field Imaging System,” J. Opt. A: Pure Appl. Opt. **5**(5), S164–S169 (2003).
4. E. R. Dowski and W. T. Cathey, “Extended Depth of Field through Wave-Front Coding,” Appl. Opt. **34**(11), 1859–1866 (1995).
5. S. Bradburn, W. T. Cathey, and E. R. Dowski, “Realizations of Focus Invariance in Optical–Digital Systems with Wave-Front Coding,” Appl. Opt. **36**(35), 9157–9166 (1997).
6. S. S. Sherif, W. T. Cathey, and E. R. Dowski, “Phase Plate to Extend the Depth of Field of Incoherent Hybrid Imaging Systems,” Appl. Opt. **43**(13), 2709–2721 (2004).
7. K. Chu, N. George, and W. Chi, “Extending the Depth of Field through Unbalanced Optical Path Difference,” Appl. Opt. **47**(36), 6895–6903 (2008).
8. T. Nobukawa, Y. Katano, T. Muroi, N. Kinoshita, and N. Ishii, “Bimodal Incoherent Digital Holography for Both Three-Dimensional Imaging and Quasi-Infinite–Depth-of-Field Imaging,” Sci. Rep. **9**(1), 3363 (2019).
9. M. R. Rai and J. Rosen, “Depth-of-Field Engineering in Coded Aperture Imaging,” Opt. Express **29**(2), 1634–1648 (2021).
10. Z. S. Hegedus, “Annular Pupil Arrays,” Opt. Acta: Int. J. Opt. **32**(7), 815–826 (1985).
11. J. Ojeda-Casta neda, P. Andrés, and A. Díaz, “Annular Apodizers for Low Sensitivity to Defocus and to Spherical Aberration,” Opt. Lett. **11**(8), 487–489 (1986).
12. J. Ojeda-Casta neda, L. R. Berriel-Valdos, and E. Montes, “Bessel Annular Apodizers: Imaging Characteristics,” Appl. Opt. **26**(14), 2770–2772 (1987).
13. E. H. Linfoot and E. Wolf, “Diffraction Images in Systems with an Annular Aperture,” Proc. Phys. Soc. B **66**(2), 145–149 (1953).
14. W. T. Welford, “Use of Annular Apertures to Increase Focal Depth,” J. Opt. Soc. Am. **50**(8), 749–753 (1960).
15. H. F. A. Tschunko, “Imaging Performance of Annular Apertures,” Appl. Opt. **13**(8), 1820–1823 (1974).
16. J. J. Stamnes, H. Heier, and S. Ljunggren, “Encircled Energy for Systems with Centrally Obscured Circular Pupils,” Appl. Opt. **21**(9), 1628–1633 (1982).
17. J. J. Stamnes, *Waves in Focal Regions: Propagation, Diffraction and Focusing of Light, Sound and Water Waves* (Routledge, 2017).
18. H. F. A. Tschunko, “Imaging Performance of Annular Apertures. 2: Line Spread Functions,” Appl. Opt. **17**(7), 1075–1079 (1978).

Optics EXPRESS

19. E. L. O'Neill, "Transfer Function for an Annular Aperture*," J. Opt. Soc. Am. **46**(4), 285–288 (1956).
20. V. N. Mahajan, "Zernike Annular Polynomials for Imaging Systems with Annular Pupils," J. Opt. Soc. Am. **71**(1), 75–85 (1981).
21. J. Ojeda-Castaneda, E. Tepichin, and A. Pons, "Apodization of Annular Apertures: Strehl Ratio," Appl. Opt. **27**(24), 5140–5145 (1988).
22. C. Sheppard and A. Choudhury, "Image Formation in the Scanning Microscope," Opt. Acta: Int. J. Opt. **24**(10), 1051–1073 (1977).
23. C. J. R. Sheppard and T. Wilson, "Depth of Field in the Scanning Microscope," Opt. Lett. **3**(3), 115–117 (1978).
24. Z. S. Hegedus and V. Sarafis, "Superresolving Filters in Confocally Scanned Imaging Systems," J. Opt. Soc. Am. A **3**(11), 1892–1896 (1986).
25. A. Lohmann, J. Ojeda-Casta neda, and N. Streibl, "Spatial Periodicities in Coherent and Partially Coherent Fields," Opt. Acta: Int. J. Opt. **30**(9), 1259–1266 (1983).
26. J. Durnin, "Exact Solutions for Nondiffracting Beams I The Scalar Theory," J. Opt. Soc. Am. A **4**(4), 651 (1987).
27. D. McGloin and K. Dholakia, "Bessel Beams: Diffraction in a New Light," Contemp. Phys. **46**(1), 15–28 (2005).
28. Z. Bouchal, "Nondiffracting Optical Beams: Physical Properties, Experiments, and Applications," Czechoslov. J. Phys. **53**(7), 537–578 (2003).
29. J. Turunen and A. T. Friberg, "Chapter 1 - Propagation-Invariant Optical Fields," in *Progress in Optics*, vol. 54 (Elsevier, 2010), pp. 1–88.
30. J. C. Gutiérrez-Vega, M. D. Iturbe-Castillo, and S. Chávez-Cerda, "Alternative Formulation for Invariant Optical Fields: Mathieu Beams," Opt. Lett. **25**(20), 1493–1495 (2000).
31. M. A. Bandres, J. C. Gutiérrez-Vega, and S. Chávez-Cerda, "Parabolic Nondiffracting Optical Wave Fields," Opt. Lett. **29**(1), 44–46 (2004).
32. Z. Bouchal, "Controlled Spatial Shaping of Nondiffracting Patterns and Arrays," Opt. Lett. **27**(16), 1376–1378 (2002).
33. A. Zannotti, C. Denz, M. A. Alonso, and M. R. Dennis, "Shaping Caustics into Propagation-Invariant Light," Nat. Commun. **11**(1), 3597 (2020).
34. B. E. A. Saleh, M. C. Teich, and M. C. Teich, *Fundamentals of Photonics* (John Wiley & Sons, Incorporated, 2013).
35. C. Snoeyink and S. Wereley, "Single-Image Far-Field Subdiffraction Limit Imaging with Axicon," Opt. Lett. **38**(5), 625–627 (2013).
36. V. Tiwari and N. S. Bisht, "Extended depth of field of a diffraction limited imaging system using a spatial light modulator based intensity compensated polarization coded aperture," Opt. Continuum **2**(1), 1–8 (2023).
37. J. W. Goodman, *Statistical Optics* (John Wiley & Sons, Incorporated, 2015).
38. "SIPI Image Database - Textures," https://sipi.usc.edu/database/database.php?volume=textures.
39. J. Boersma, "On the Computation of Lommel's Functions of Two Variables," Math. Comput. **16**(78), 232–238 (1962).
40. J.-B. Sibarita, *Deconvolution Microscopy*, Advances in Biochemical Engineering (Springer, 2005).
41. M. Born, *Principles of Optics: Electromagnetic Theory of Propagation, Interference and Diffraction of Light* (Pergamon Press, 1980).